Radiometric Characteristics of KOMPSAT-3 Multispectral Images Using the Spectra of Well-Known Surface Tarps

Jong-Min Yeom, Jisoo Hwang, Cheong-Gil Jin, Dong-Han Lee, and Kyung-Soo Han

Abstract—**A vicarious calibration with reference to characterized surface tarps was conducted to determine the first radiometric characteristics of KOMPSAT-3. The 6S radiative transfer model was also used by inputting various initial parameters, such as the spectral response function of KOMPSAT-3, and atmospheric and geometric conditions. Moderate-Resolution Imaging Spectroradiometer atmospheric products, such as aerosol optical depth, precipitable water, and total ozone, were used as input parameters to interpret solar radiation reflection, scattering, and absorption effects. In the first field campaign, the radiometric coefficients from each of the spectral bands were estimated by calculating the predicted radiance at sensor level and the digital number (DN) of KOMPSAT-3 based on a linear least squares fit over a range of target reflectance levels. The second field campaign measurements were also used to upgrade the KOMPSAT-3 DNs to radiance coefficients. The root-mean-square error differences between simulated radiance and measured radiance during the second field campaign for "sensor-to-itself" calibration were 2.072 W/m^{2}sr (blue), 6.80 W/m^{2}sr (green), 7.512 W/m^{2}sr (NIR), and 5.712 W/m^{2}sr (red), respectively. This highlights that radiometric calibration with tarps is a reliable method. Furthermore, the gain ratio between the first and the second one was $< 5\%$, indicating reasonable radiometric calibration results. Additionally, cross-validation of KOMPSAT-3 with radiometrically well-calibrated Landsat-8 was performed over bright desert. Although the difference between the vicarious calibration with surface tarps and cross-validation with Landsat-8 was significant, reasonable results were obtained under close geometrical conditions, despite inherent vicarious calibration error.**

Index Terms—**Cross-calibration, Korea Multi-Purpose Satellite-3 (KOMPSAT-3), Moderate-Resolution Imaging Spectroradiometer (MODIS), radiometric calibration, surface tarp, vicarious calibration.**

I. Introduction

THE Korea Multi-Purpose Satellite-3 (KOMPSAT-3), developed by the Korea Aerospace Research Institute (KARI), was launched on May 18, 2012, from the Tanegashima Space Center of the Japan Aerospace Exploration Agency (JAXA), Japan, on an H2A launch vehicle. KOMPSAT-3 covers the spectral range from blue (450–520 nm), green (520–600 nm), and red (630–690 nm) to the near infrared (760–900 nm) with a 2.8-m spatial resolution, whereas the panchromatic imagery (450–900 nm) has a 0.7-m geometric resolution and a swath width of 15 × 15 km at nadir. Under normal mission operations, the KOMPSAT-3 imaging modes consist of strip, multipointing, single-pass stereo imaging, wide-area along imaging, and arbitrarily wide imaging. For strip imaging, the spacecraft is slewed about the roll and pitch axis into the reference attitude before imaging is initiated. During imaging, this reference attitude is kept nearly constant. Yaw steering is performed to enhance the image quality. Multipoint imaging collects images from several positions, forward and backward, and to either side of the satellite, in a single pass; image collection is initiated once the satellite achieves the required roll and pitch. Single-pass stereo imaging collects a stereo image of the target during a single pass; tilt into the required roll and pitch direction is executed while maneuvering. Arbitrarily wide-area imaging widens the swath by taking advantage of the satellite's maneuverability; in this case, two consecutive scenes that lie side by side, but not in the flight direction, are imaged.

The primary purpose of the KOMPSAT-3 mission, which is a continuation of the KOMPSAT-1 and 2 earth observation satellite programs, is to meet the nation's need for high-resolution electrooptical imagery for GIS and other environmental, agricultural, and oceanographic monitoring applications. To accomplish the suggested mission purposes, especially for quantitative applications such as vegetation index, leaf area index, carbon monitoring, and crop management, the potential user groups require reliable radiometric information.

Monitoring the radiometric characteristics of satellite sensors is an essential step in the estimation of reliable continuous variables for quantitative applications, such as a vegetation index, leaf area index, and albedo. This radiometric calibration, which converts the electronic digital number (DN) values to physical units, has been performed to acquire consistently accurate radiometric information over a specifically designed sensor's lifetime [1], [2]. To secure radiometric calibration and the continuity of satellite data from multiple sensors, pre- and postlaunch calibration has been proposed to determine the characteristics of radiometric calibration [3]–[5]. The precalibration step, which is conducted in a controlled laboratory setting, uses a well-characterized radiant source. However, because calibrated sensors are degraded by the severe environmental conditions encountered after launch [6], operational spaceborne satellites

need to be monitored to obtain their absolute radiometric characteristics when in orbit. For in-flight calibration of satellites, onboard, vicarious, lunar, and cross-calibration techniques have been suggested for radiometric calibration [7]–[12]. Onboard calibration is performed in orbiting satellites using well-known sources such as artificial lamps or the sun. Onboard calibrators have the advantage of allowing frequent response determinations. However, they increase the cost and weight of instruments. Vicarious and cross-calibration techniques are used for systems without onboard calibrators. These techniques also act as a validation tool for systems with onboard calibrators [9], [10], [13].

In this paper, the vicarious calibration method, relying on *in situ* characterizations of surface targets, was applied to monitor the initial radiometric characteristics of KOMPSAT-3. The radiometric characteristics of KOMPSAT-3 were not previously defined because KARI has primarily focused on spatial and geometrical issues rather than absolute radiometric calibration. Furthermore, it is difficult to obtain atmospheric and surface measurements during the early operational period. Eventually, field campaigns were conducted, in South Korea, to obtain hyperspectral surface reflectances using handheld radiometric instruments. Several important campaign conditions were necessary, such as characterizations without cloud cover and a flat homogeneous surface. When applying a radiative transfer model, information regarding atmospheric constituents, such as aerosol optical depth, ozone column, and water vapor content, was collected with well-validated Moderate-Resolution Imaging Spectroradiometer (MODIS) products from NASA's Earth Observing System Data and Information System (EOSDIS) because we did not prepare the affiliated instruments such as sun photometer Microtops to measure atmospheric products during the field campaigns. The vicarious calibration methodology using Second Simulation of the Satellite Signal in the Solar Spectrum (6S) radiative transfer simulations, based on MODIS atmosphere products, is effective for practical, rapid, and low-cost radiometric calibration, with a 7% error degree of accuracy [9]. The aim of our study was to characterize KOMPSAT-3 absolute radiometric calibration after in-orbit testing with limited data to determine the initial condition of the Advanced Earth Imaging Sensor System (AEISS).

II. MATERIALS AND METHODS

KOMPSAT-3 provides 2.8-m ground sample distance (GSD) multispectral images and 0.7-m GSD panchromatic images under a nominal orbit. The designed lifetime of the satellite mission is four years. A detailed summary of KOMPSAT-3 is given in Table I.

The study area was located in Goheung County, South Korea [34.60° N, 127.20° E; Fig. 1(a)]. Based on ground measurements of the climate for the last 30 years from the Korea Meteorological Agency (KMA), this region has a moderate marine climate with a low daily temperature range. The annual mean temperature is 13.6 °C. The annual precipitation and humidity are 1453.4 mm and 69%, respectively [14].

A pair of KOMPSAT-3 multispectral images was acquired on April 12, 2013, at 04:34 coordinated universal time (UTC) and on February 21, 2014, at 04:41 UTC [Fig. 1(b) and (c)]. The acquisition from the first field campaign was used to set the

TABLE I
DETAILED SUMMARY OF KOMPSAT-3

Mission characteristic	Information
Design lifetime	4 years
Weight of satellite	≈ 980 kg
Orbit altitude	685 km
Swath width	15 km (at nadir)
Ground sample distance	Panchromatic band: 0.7 m (altitude 685 km) Multi spectral bands: 2.8 m (altitude 685 km)
Spectral bands	Pan 450–900 nm Blue 450–520 nm Green 520–600 nm Red 630–690 nm NIR 760–900 nm

initial conditions of KOMPSAT-3 radiometric calibration by estimating the DNs to radiance conversion coefficients [Fig. 1(b)]. The measurements made in the second campaign were used to validate the initial coefficient estimates and to upgrade the KOMPSAT-3 DNs to radiance coefficients with the spectral reflectance acquired for tarps and MODIS products [Fig. 1(c)]. In Fig. 1(b), a total of eight surface tarps (each with an area of 10×10 m) were used to acquire the precise surface reflectance corresponding to the red square in Fig. 1(a). When measuring the spectral reflectance of surface tarps, KOMPSAT-3 overpass times were carefully considered to ensure a less than 30-min difference to reduce atmospheric and geometric discrepancies. In the case of the second field campaign, four bigger tarps (each with an area of 10×20 m) were used. The reason that we prepared larger tarps than those used in the first field campaign was to reduce the adjacency effects induced by closely located tarps for purely reflected spectral radiance on tarps. The adjacency effects would not only be emerged by the environmental reflectance of the target but also be interfered by surrounding pixels due to the point spread function (PSF) of KOMPSAT-3 multispectral bands. In the case of KOMPSAT-3, although the maximum pixel size of PSF refers as 4 pixels [15], it is difficult to precisely define the effects of PSF. In this paper, we just mentioned the potential sources of error by PSF and did not consider to correct PSF effects of KOMPSAT-3 multispectral bands due to technical limitation. The white numbers on the tarps in Fig. 1(b) and (c) coincide with the numbers identifying the spectral curves in Fig. 2(b) and (c), respectively.

KARI field campaigns were performed by measuring the surface spectral reflectance with a handheld ASD FieldSpec 3 full-range spectroradiometer in Goheung County, South Korea. The ASD FieldSpec 3 has a 3-nm spectral resolution covering 350–1000 nm and a 10-nm spectral resolution in the 1000–2500-nm spectral range. Before the measurement of targets by KARI, we changed the averaging sets to at least 30 for all spectra, dark current, and white reference to improve the signal-to-noise ratio of our spectra. To consider changeable field conditions, optimization adjustments, dark correction collection, and white reference scan were conducted to obtain reliable target reflectance. In the case of white reference target, Spectralon which was calibrated by PANalytical Company was used.

In this paper, to simulate radiance at sensor levels, the 6S radiative transfer model [16] was used by considering the spectral response function (SRF) of KOMPSAT-3, atmospheric
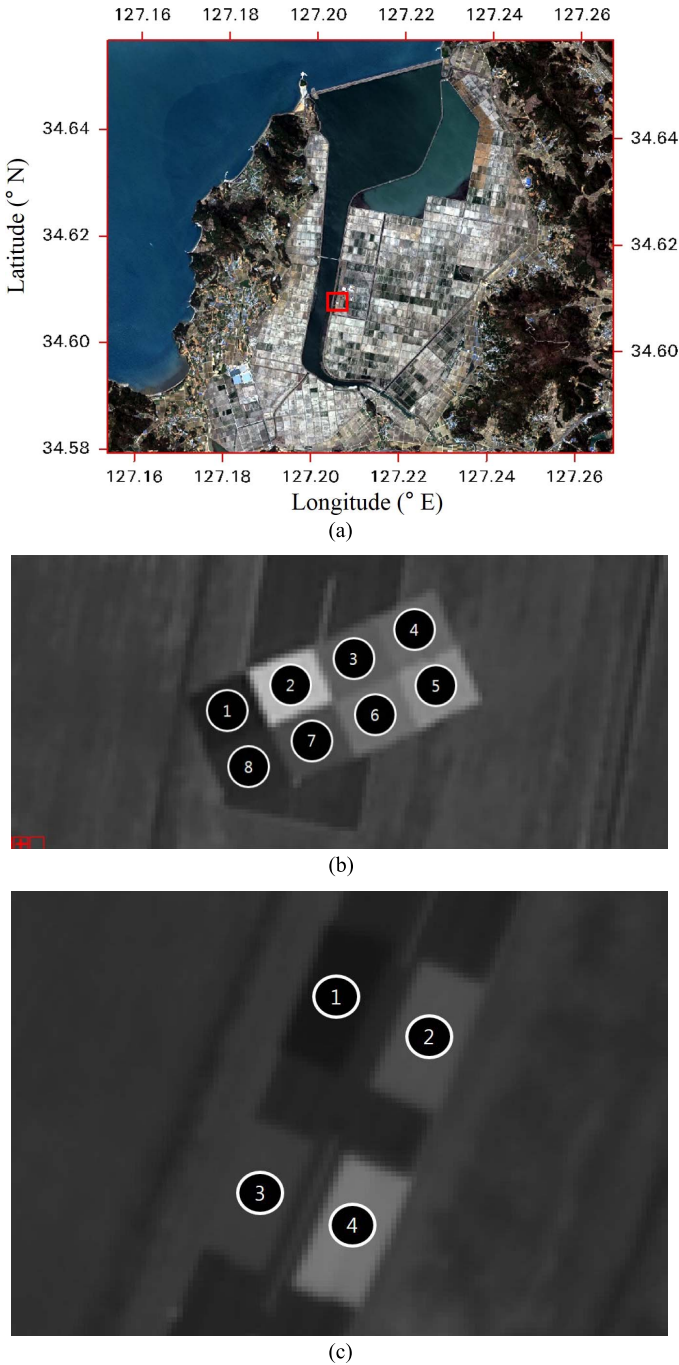
Fig. 1. (a) Cropped KOMPSAT-3 RGB image from the western area of South Korea on April 12, 2013. (b) and (c) show the locations of surface tarps for a known-reflectance spectroradiometer corresponding to the red square in (a).

and geometric conditions, background surface reflectance, and spectral reflectance of surface tarps. When considering background surface reflectance, surface spectral libraries of the Korean Institute of Geoscience and Mineral Resources were used. The geometric conditions of KOMPSAT-3 during the two field campaigns, including the data acquisition date, solar zenith angle, solar azimuth angle, viewing zenith angle, and viewing azimuth angle, are represented in Table II, which was obtained from Metafiles.

For the atmospheric parameters, we utilized MODIS atmospheric products, such as aerosol optical depth, aerosol
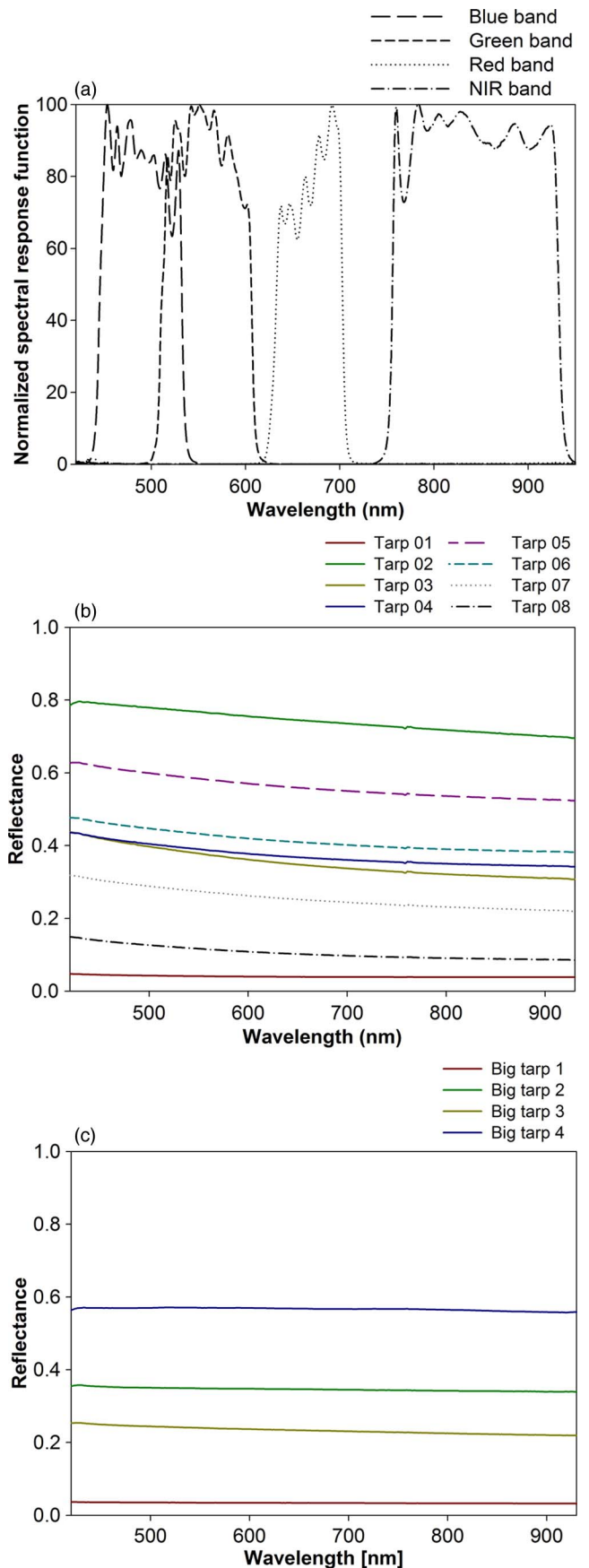

Fig. 2. (a) Relative SRF curves for KOMPSAT-3. Measured surface tarp reflectances using a spectroradiometer for the (b) first and (c) second field campaigns.

TABLE II
GEOMETRIC CONDITIONS OF KOMPSAT-3 FOR VICARIOUS CALIBRATION

Date	Overpass time (UTC)	Solar zenith	Solar azimuth	Viewing zenith	Viewing azimuth	Nominal GSD(m)
April 12, 2013	04:34:52	26.32	178.06	10.34	112.01	2.865
February 21, 2014	04:41:20	45.97	174.7294	1.319	137.47	2.849

TABLE III
ATMOSPHERIC CONDITIONS OF KOMPSAT-3 FOR 6S SIMULATION

Date	Aerosol optical depth (550 nm)	Standard aerosol model	Water vapor (g/cm^2)	Ozone (cm-atm)
April 12, 2013	0.061	Maritime	0.718	0.5353
February 21, 2014	0.088	Maritime	0.292	0.3640

Fig. 3. Schematic of hyperspectral gonioreflectometer for BRDF measurements on tarps [17].

type, total ozone, and total precipitable water, as input values in a simulation model. We used these MODIS products instead of using precise ground measurements because the affiliated instruments were not available. The aim of this study was to obtain the initial radiometric conditions of KOMPSAT-3, within a 10% degree of accuracy. The following MODIS/Terra daily Level 2 and Level 3 atmospheric products were considered: MOD04_L2 (data field of "Optical_Depth_Land_And_Ocean" and "Aerosol_Type_Land"), MOD05_L2 (data field of "Water_Vapor_Near_Infrared"), and MOD07_L2 (field of "Total_Ozone") for gaseous absorption by ozone, water, and scattering by Rayleigh scattering and aerosols. Because these MODIS products have different spatial resolutions, the pixels nearest the study location were selected for 6S simulation. The atmospheric conditions used for KOMPSAT-3 in the 6S simulation corresponding to the tarp area are given in Table III. The aerosol optical depths at 550 nm during the first and second field campaigns were 0.061 and 0.088, respectively. The time difference between KOMPSAT-3 and MODIS was less than 3 h. We used the geostationary satellite RGB images during the field campaign periods to check for cloud effects and found periods of clear sky for the duration of daylight hours. For the aerosol model, maritime type was selected. This is the default standard aerosol 6S model.

To reflect the characteristics of KOMPSAT-3 spectral bands, the normalized SRFs in steps of 2.5 nm were also used as inputs in the 6S radiative transfer model in Fig. 2(a). This is similar to the SRF function patterns used in other high-resolution satellites, such as IKONOS, GeoEye, and KOMPSAT-2. Fig. 2(b) shows the spectral reflectance of tarps measured with ASD FieldSpec. As shown in Fig. 2(b), all of the spectral reflectance curves at 1-nm resolution vary with wavelength, with the exception of the bottom curve that has a spectrally flat pattern. The spectral curves from the four tarps of the second field campaign are also shown in Fig. 2(c), with a more stable pattern than that shown for the first campaign. This is because it was painted using different chemical compounds, which have only recently received approval for use in South Korea. The details of these compounds are confidential because the big tarps were developed by the defense industry. For the input parameters of the 6S simulation, each spectral curve with 1-nm resolution from ASD FieldSpec was resampled to 2.5 nm according to the KOMPSAT-3 spectral band wavelength range.
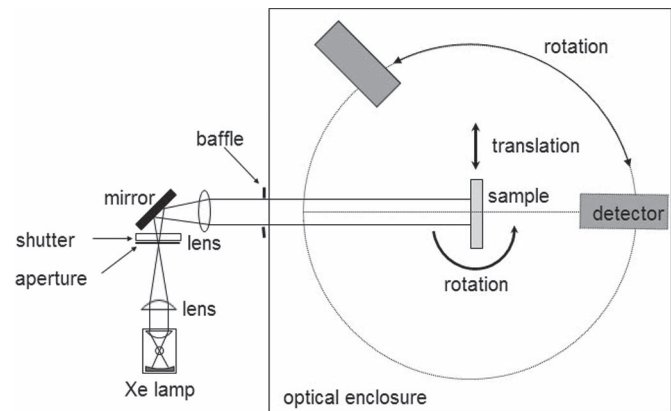
The spectral wavelength ranges (400–1000 nm) of the surface tarps cover the KOMPSAT-3 multispectral wavelength range (from blue to NIR bands); this result shows that surface tarp data provide reliable surface reference data of KOMPSAT-3 multispectral bands. When measuring spectral reflectance of radiometric tarps with ASD FieldSpec, we carefully observed the nadir direction on the surface targets to reduce the anisotropy effects and angular discrepancy within the satellite observation geometry.

To quantify the BRDF effects of the surface tarps, we used a gonioreflectometer for absolute measurements of the hyperspectral and angular reflectance at four of the radiometric tarps (which were used as reference surface tarps) during the second field campaign. We cut each radiometric tarp into 30 × 30 cm parts and measured the BRDF of each tarp under laboratory experimental conditions. Fig. 3 shows a schematic of the BRDF measurement instrument, which consists of a source system and a goniometric detection system. The gonioreflectometer determined BRDF values of the tarps in wavelengths between 450 and 1000 nm with a 1-nm spectral resolution using a white source and a charge-coupled device (CCD) based spectroradiometer. A detailed description of the laboratory BRDF instrument is described in a previous report [17]. The instrument can measure only in the principle plane direction, which indicates that it is impossible to interpret the BRDF effects of azimuth direction according to relative sensor–tarps–sun geometry.

A full description of our laboratory-based analysis of BRDF measurements of radiometric tarps is beyond the scope of this paper. However, we have presented previous research of laboratory-based BRDF calibration of radiometric tarps [18]. We have focused on quantifying the effects of anisotropy on the radiometric tarps during the field campaign. First of all, we estimated the laboratory-based BRDF of tarps in a range from 450 to 1000 nm with 1-nm spectral interval. The illumination
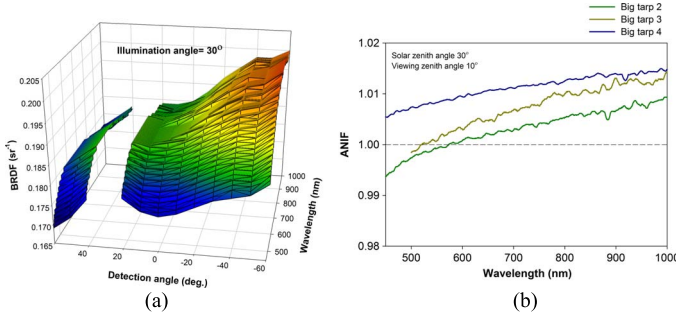
Fig. 4. (a) is the BRDF measurement laboratory-based BRDF measurement of the highest reflectance tarps (∼60%) under 30° illumination angle condition. (b) is the ANIF values of each big tarp from BRDF using a hyperspectral gonioreflectometer.

angle has ranges from 0° to 60° with 10° resolution. For each illumination angle condition, the viewing angle is in a range from −60° to 60° with 10° interval. Fig. 4(a) shows the sample of laboratory-based BRDF measurement of the highest reflectance tarps (∼60%). The discontinuity areas in Fig. 4(a) were showed under the same illumination and detection angle condition due to the characteristics of the hyperspectral gonioreflectometer. The asymmetric BRDF pattern was showed in a 3-D mesh figure, indicating that the BRDF effects of the azimuth direction would be expected. Based on the BRDF measurements of sampled big tarps, we estimated the anisotropy factor (ANIF) to interpret geometry-related BRDF differences between nadir measurements with ASD FieldSpec geometry and KOMPSAT-3 observation geometry. ANIF [19] is defined as

$$\text{ANIF}(\varphi_i, \theta_i; \varphi_r, \theta_r; \lambda) = \frac{\text{BRDF}(\varphi_i, \theta_i; \varphi_r, \theta_r; \lambda)}{\text{BRDF}_N(\varphi_i, \theta_i; \varphi_r, \theta_N; \lambda)} \quad (1)$$

where $\text{BRDF}(\varphi_i, \theta_i; \varphi_r, \theta_r; \lambda)$ is the BRDF for incident radiance that comes from the azimuth (φ_i) and elevation (θ_i) directions, which is reflected to the azimuth (φ_r) and elevation directions (θ_r) at wavelength λ. $\text{BRDF}_N(\varphi_i, \theta_i; \varphi_r, \theta_N; \lambda)$ is measured at the nadir direction, where $\theta_N = 0°$. This equates to unity for all φ_r at all λ. We estimated ANIF by dividing $\text{BRDF}(\varphi_i, \theta_i; \varphi_r, \theta_r; \lambda)$ with a 30° solar zenith angle and a −10° viewing zenith angle into $\text{BRDF}_N(\varphi_i, \theta_i; \varphi_r, \theta_N; \lambda)$ with a nadir viewing zenith angle. This was performed to better understand the BRDF effects of the radiometric tarps on the KOMPSAT-3 radiometric calibration. That is to say, we used the ANIF values to quantify the BRDF effects of the radiometric tarps when performing the radiometric calibration of KOMPSAT-3, indicating the maximum viewing zenith angle.

As shown in Fig. 4(b), the ANIF values of all big tarps from the second field campaign showed negligible BRDF effects of tarps in spite of a 10° viewing zenith angle with 30 illumination angle. The maximum value of ANIF is about 1.5% over the highest reflectance big tarp 2 [dark blue line in Fig. 4(b)]. ANIF values were getting higher as the value of the wavelength increased for all big tarps. When determining the expected degree of radiometric accuracy, we have allocated error values and assumed a Lambertian reflection for radiometric tarps to 1.5%. A laboratory-based BRDF correction from the hyperspectral gonioreflectometer was not applied for several reasons. First, we found that the BRDF effects of the azimuth angle direction are expected because asymmetric BRDF patterns appeared in
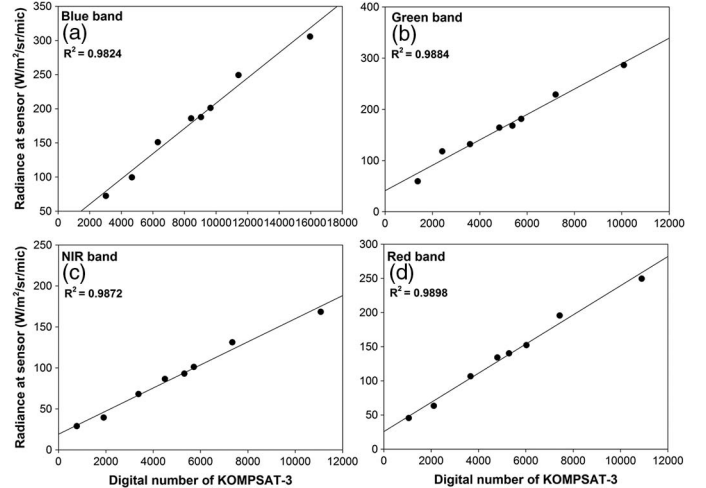

Fig. 5. Scatter plots of KOMPSAT-3 DNs and simulated radiance at the sensor for all spectral bands during the first field campaign. (a)–(d) show blue, green, NIR, and red bands, respectively.

radiometric tarps. As mentioned before, a hyperspectral gonioreflectometer can only measure the BRDF of tarps over the principal plane. Second, it is difficult to measure BRDF due to a low signal-to-noise ratio of the low reflectance tarps (∼3%) [Fig. 1(c)]. Finally, in the case of eight of the small tarps for the first field campaign, no measurements were possible because they were damaged. Therefore, the surface tarps in the measurement sites were assumed to be Lambertian due to those low BRDF effects.

III. Results

A. Radiometric Calibration of KOMPSAT-3 With Surface Tarps

The simulated radiance from the 6S radiative transfer model at the top of the atmosphere (TOA) was matched with KOMPSAT-3 DNs and was used to obtain radiance coefficients, based on a linear least squares fit of radiance versus tarp reflectance. Fig. 5 shows a scatter plot comparison between simulated radiances and KOMPSAT-3 DNs. All of the KOMPSAT-3 spectral bands showed linear patterns. Most of the plots between DN and radiance for the eight surface tarps were located close to the linear least squares fit lines, with a coefficient of determination of more than 0.9 R^2 for all bands. The red band had the highest R^2 value, while the blue band had the lowest. Scatter plot results indicated that the use of tarps, measured for surface reflectance during each field campaign, could generate radiometric coefficients. Despite the linear relationship, similar scattered patterns were apparent for all spectral bands. We speculate that adjacency effects induced by closely laid tarps were responsible for the scattered pattern, despite the 10×10 m tarp sizes. Therefore, to reduce the adjacency effects between small tarps, we prepared larger tarps during the second field campaign using a different paint compound.

Table IV shows the initial estimated radiometric calibration coefficients (scale factor and offsets) from KOMPSAT-3 DNs and the corresponding R^2 for each spectral band.

In this paper, the exo-atmospheric solar spectral irradiances (ESUN_λ) were also calculated for each of the KOMPSAT-3

TABLE IV
INITIAL ESTIMATED RADIOMETRIC CALIBRATION COEFFICIENTS
(SCALE) FROM KOMPSAT-3 DNs AND ESUN Λ DURING
THE FIRST FIELD CAMPAIGN

Spectral band	Scale factor	Offset	R^2	ESUN$_\lambda$[1] (W/m^2·μm)
Blue	0.0185	23.3642	0.9824	1970.281
Green	0.0248	41.2829	0.9789	1814.155
NIR	0.0141	19.0661	0.9872	1024.850
Red	0.0214	25.6187	0.9898	1516.303

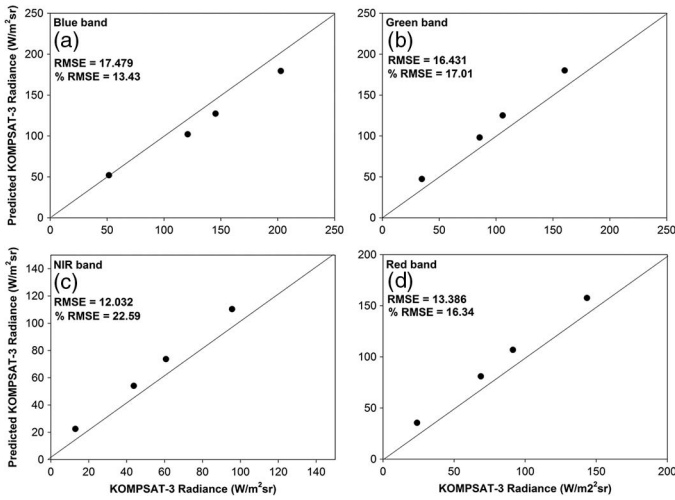[1]Exo-atmospheric solar spectral irradiance.

Fig. 6. Scatter plots of measured KOMPSAT-3 TOA radiance using the radiance coefficients derived from the first campaign and the predicted KOMPSAT-3 radiance over tarp surface reflectance used in the second field campaign: (a)–(d) show blue, green, NIR, and red bands, respectively.

spectral bands by integrating the SRF$_\lambda$ of each band [Fig. 2(a)] with the corresponding solar irradiance (Table IV)

$$\text{ESUN}_\lambda = \frac{\int (\text{SRF}_\lambda \cdot \text{Solar irradiance}) d\lambda}{\int \text{SRF}_\lambda d\lambda}. \qquad (2)$$

Solar irradiance from 250 to 4000 nm (in steps of 1 nm) was used to estimate ESUN$_\lambda$ following [20]. The retrieved ESUN$_\lambda$ was used to generate the TOA reflectance, with radiance calibration coefficients estimated from the DNs of KOMPSAT-3 spectral bands.

In the second field campaign, the model results from the use of the 6S model were compared to the measured radiance using radiometric calibration coefficients from the first campaign. The values were converted from DN with the initially determined radiance calibration coefficients. The predicted KOMPSAT-3 radiances of each band from the use of the 6S direct radiative transfer model were estimated using the surface spectral reflectance of radiometric tarps, geometric condition, and atmospheric conditions. The scatter plots of the predicted KOMPSAT-3 TOA radiance from the 6S model and measured KOMPSAT-3 TOA radiance based on the initial radiometric calibration coefficients are shown in Fig. 6. For all of the KOMPSAT-3 spectral bands, most of the plotted points were located close to the reference line, which had a slope of 1.0. The root-mean-square error (rmse) and percentage rmse were also
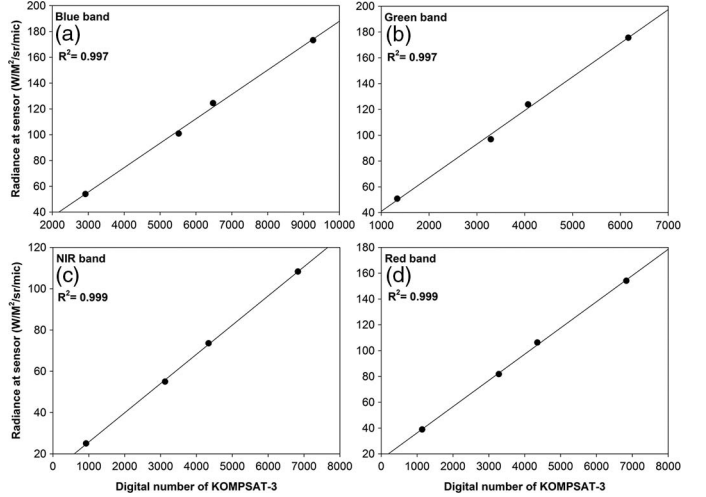

Fig. 7. Scatter plots of KOMPSAT-3 DNs and simulated radiance at the sensor for all spectral bands during the second field campaign: (a)–(d) show blue, green, NIR, and red bands, respectively.

calculated. The most accurate percentage rmse was obtained for the blue band (13.43%), while the NIR band had the largest discrepancy. All of the percentage rmse values for plots between KOMPSAT-3 and tarp surface reflectance were less than 22%. We inferred that the primary sources of radiance discrepancy for each band are due to disparate atmospheric conditions between the two field campaigns (despite using MODIS atmospheric products) and adjacent effect of tarps. Although there was a 22.595% difference in the NIR band, the radiometric coefficients that were determined initially are still considered useful for estimating KOMPSAT-3 multispectral surface reflectance.

Based on the measurements made in the second field campaign, we also upgraded KOMPSAT-3 DNs to radiance coefficients from the 6S radiative model using the same method and data formulation as that adopted in the first field campaign. We expected that using a larger tarp and a decreased viewing zenith angle would enable radiance coefficients to be reliably obtained from DNs due to the reduced adjacency effects. As shown in Fig. 7, the scatter plot relationship between the simulated radiance at the sensor and KOMPSAT-3 DNs was better represented than in the first field campaign (Fig. 5). The blue band had the lowest R^2 value (0.997), and NIR had the highest (0.999). All of the R^2 values for the spectral bands from the second field campaign were improved compared to the previous results, indicating that reducing the adjacency effects by using bigger tarps and a decreased viewing zenith angle was effective for determining the radiometric coefficients.

Table V lists the estimated radiometric calibration coefficients from KOMPSAT-3 DNs and percentage rmse during the second field campaign.

In this paper, "sensor-to-itself" calibration was performed to validate the method described in [21]. In other words, the measured radiances from DN to radiance coefficients during the second field campaign were compared to simulated KOMPSAT-3 radiances from the 6S model with affiliated atmospheric products. For all bands, the rmse indicated a reasonable accuracy. The accuracy of the blue band showed the greatest accuracy (2.072 W/m^{2}sr), while the NIR band exhibited an accuracy of 7.512 W/m^{2}sr (Table V).

TABLE V
ESTIMATED RADIOMETRIC CALIBRATION COEFFICIENTS (SCALE)
FROM KOMPSAT-3 DNs AND PERCENTAGE RMSE
DURING THE SECOND FIELD CAMPAIGN

Spectral band	Scale factor	Offset	RMSE [W/m^{2}sr]	Gain ratio between first and second field campaign
Blue	0.0189	-1.211	2.072	0.978
Green	0.0261	15.000	6.800	1.052
NIR	0.0142	11.610	7.512	0.993
Red	0.0203	15.980	5.712	1.054

TABLE VI
APPROXIMATE ERROR BUDGET FOR THE VICARIOUS
CALIBRATION OF KOMPSAT-3

	Accuracy %	Radiance error %
Relative radiometric correction	5%	5%
Solar irradiance data	3%	3%
Surface reflectance measurement	1%	1%
Lambertian assumption of surface tarps	1.5%	1.5%
ASD FieldSpec® 3 instrument	1%	1%
6S Radiative transfer	1%	1%
Aerosol optical depth from MODIS	< 0.25	2%
Total ozone from MODIS	20%	1%
Column water-vapor amounts from MODIS	20%	1%
Combined error		~ 7%

Finally, we also estimated the gain ratio between the first and second field campaigns. All bands showed a discrepancy of less than 5%, with the highest seen in the red band (Table V). These statistical results indicate that the radiometric coefficients determined for KOMPSAT-3 are suitable for estimating surface reflectance. Specifically, they should prove useful for user groups that estimate continuous variables for quantitative applications.

B. Approximate Error Budget

Table VI lists the approximate error budget from the major source of radiometric uncertainty for KOMPSAT-3 calibration. When estimating the approximate error budget of KOMPSAT-3, we simply assigned a worse case uncertainty to remind the user that these errors exist. Detailed descriptions of the error uncertainties are discussed as follows. Basically, before distributing satellite products to the user, KARI performs a detector-relative radiometric correction process for uniformity of sensor images because the assembled CCD sensor of AEISS generally has variations between detectors, which appear in the along-track direction of scanning. The relative radiometric accuracy specification of KOMPSAT-3, determined during in-orbit testing, is less than 5%. In this paper, we did not utilize the effect of the relative radiometric correction process for the results of absolute calibration; instead, we focused on the final user distribution products of KOMPSAT-3.

Other major error sources for absolute radiometric calibration include those related to surface reflectance measurements of the tarps with ASD FieldSpec 3. When inputting the surface reflectance of the tarps to the 6S model, the surface reflectance resampled as 2.5 nm is used, despite the fact that peak-to-peak reflectance variation exists within each band of the spectral wavelength range; the variation is less than 1% for each spectral band. Additionally, non-Lambertian surface tarps were also introduced and based on laboratory-based BRDF measurements. We assigned a 1.5% error accuracy for assuming a Lambertian target surface tarp based on prior experimental results.

Table VI lists additional information on atmospheric constituents' sensitivity, accuracy of MODIS atmospheric products for aerosol optical depth [22], [23], column water vapor amounts [24], and total ozone [25]. In this paper, TOA radiances from the 6S model on February 21, 2014, were simulated with extreme error range values by considering additional temporal discrepancy from aerosol, ozone, and water vapor values to determine the radiance error in the MODIS products used. The expected error of each MODIS atmospheric product was less than 2.4%.

Assuming that the aforementioned major error sources are independent, the combined error value for the vicarious calibration of KOMPSAT-3 is approximately 7%.

C. Cross-Comparison With Landsat-8 OLI With Determined Radiometric Coefficients

In this paper, the calibrated KOMPSAT-3 sensor with surface tarps was also validated using the radiometrically stable Landsat-8 Operational Land Imager (OLI) [26], which is considered a reference sensor for the evaluation of the radiometric characteristics of KOMPSAT-3. The radiometric accuracy of Landsat-8 OLI is typically within 3% for all reflective bands, which range from visible to short-wave infrared [27]. The historical selection of 20 desert areas, carefully selected for reference standard test sites by Cosnefroy et al. [28], was used for cross-validation of KOMPSAT-3 with Landsat-8 OLI. These target areas were used for cross-validation, based on the stability and homogeneity criteria of the desert area [29], [30]. Also, low cloudiness and characterized BRDF behavior were useful for cross-calibration [28]. In this paper, we referred to cross-validation methods used in previous studies [21], [31]. We briefly describe the method of cross-validation for KOMPSAT-3 with Landsat-8 as follows. Before performing cross-validation over 20 desert sites, the geometrical conditions of KOMPSAT-3 and Landsat-8 were considered to reduce not only the effect of the bidirectional behavior of the surface but also the atmospheric contribution on radiative transfer simulation. Basically, it is difficult to acquire the same geometrical

TABLE VII
GEOMETRIC CONDITIONS OF KOMPSAT-3 AND LANDSAT-8 FOR CROSS-VALIDATION

Sites	Date		Solar zenith (azimuth) angle		Viewing zenith (azimuth) angle	Nominal GSD (m)
	KOMPSAT-3	Landsat-8	KOMPSAT-3	Landsat-8	KOMPSAT-3	KOMPSAT-3
Algeria-3	2014/12/28 12:40	2014/12/28 10:02	56.05 (199.25)	57.59 (155.46)	27.20 (321.92)	3.365
Libya-4	2015/03/05 11:17	2015/03/05 08:54	35.92 (196.44)	42.52 (140.97)	31.23 (78.91)	3.463
Libya-4	2015/03/21 11:40	2015/03/21 08:54	32.48 (211.81)	36.80 (136.58)	17.32 (261.68)	2.984
Libya-4	2014/04/03 11:33	2014/04/03 08:55	27.70 (215.49)	32.05 (132.42)	11.31 (80.16)	2.867
Libya-4	2014/09/10 11:29	2014/09/10 08:55	28.14 (216.51)	31.38 (135.26)	9.43 (80.22)	2.904
Libya-4	2013/06/03 11:40	2013/06/03 08:57	18.17(254.15)	20.32(103.33)	1.21(260.50)	2.799
Libya-4	2013/08/06 11:39	2013/08/06 08:57	19.27(235.97)	24.64(114.37)	1.93(80.78)	2.799

conditions due to the different observation characteristics of the sensors. Furthermore, the KOMPSAT-3 equatorial crossing time, which is 13:30 P.M. local time (ascending node), is different from that of Landsat-8, which is 10:00 A.M. local time (descending node). During the year following vicarious calibration with a surface tarp, we searched and obtained only seven matched datasets of geometrically coupled KOMPSAT-3 and Landsat-8 data from 20 desert sites, as listed in Table VII.

With geometrically coupling data sets, corresponding subset areas with 300 × 300 m from KOMPSAT-3 and Landsat-8 were selected based on visual inspection to acquire the homogenous areas among desert sites. In the case of KOMPSAT-3, a total of 110 × 110 pixels were used, while Landsat-8 OLI was 10 × 10 pixels. Each selected subset area for DNs and TOA radiance was averaged to reflect the difference in spatial resolution and reduce interference of environmental pixels by the PSF. Fig. 8 is a schematic of the cross-validation steps between the Landsat-8 OLI and KOMPSAT-3 over desert areas. Once matching measurements between KOMPSAT-3 and Landsat-8 OLI were determined, the surface reflectance of Landsat-8, considered as a reference, was calculated using the inversion model of the 6S radiative transfer model from the top atmospheric reflectance of Landsat-8 OLI. Generally, because the SRFs of each band from "reference sensor" and "sensor to calibrate" are strictly different, spectral resampling should be executed to estimate the corresponding surface reflectance of "sensor to calibrate." In this paper, we utilized a spline function to model the spectral behavior of the desert sites, which is represented as a smooth
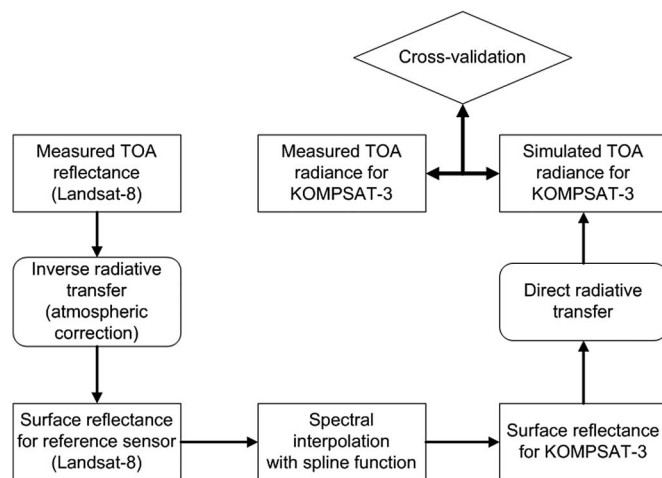

Fig. 8. Schematic of cross-validation steps between KOMPSAT-3 and Landsat-8 over desert areas.

curve between spectral bands of the reference sensor [21]. For spectral interpolation, continuous reflectance profiles of the references are computed using a spline function with all of the Landsat-8 OLI measurements. The KOMPSAT-3 sensor reflectance is estimated by integrating this profile into the KOMPSAT-3 SRF [31]. In the case of atmospheric measurements, water vapor data from the National Centers for Environmental Prediction (NCEP) and ozone data from the Ozone

TABLE VIII
TOA RADIANCE RESULTS USING UPDATED CROSS-VALIDATION OVER SELECTED DESERT AREAS

Site (Date)	Band	DN	TOA radiance [W/(m²sr)]	KOMPSAT-3 Radiance [W/(m²sr)]	Percent difference (%)
Algeria-3 (2014/12/28)	Blue	4367	63.706	82.099	-25.230
	Green	4171	89.215	123.863	-32.521
	Red	6373	112.088	145.351	-25.842
	NIR	7181	85.529	113.580	-28.176
Libya-4 (2015/03/05)	Blue	7824	127.459	147.091	-14.301
	Green	7057	154.188	199.187	-25.468
	Red	9656	177.948	211.996	-17.463
	NIR	10433	131.047	159.758	-19.746
Libya-4 (2015/03/21)	Blue	7824	134.865	147.091	-8.672
	Green	6804	162.287	192.584	-17.075
	Red	9237	180.675	203.491	-11.878
	NIR	10034	139.959	154.092	-9.613
Libya-4 (2014/04/03)	Blue	7502	136.475	141.037	-3.288
	Green	6707	168.91	190.052	-11.779
	Red	9203	198.987	202.800	-1.898
	NIR	10200	130.407	156.450	-18.157
Libya-4 (2014/09/10)	Blue	7456	133.281	140.172	-5.040
	Green	6585	163.812	186.868	-13.149
	Red	9026	198.754	199.207	-0.228
	NIR	9658	122.024	148.753	-19.742
Libya-4 (2013/06/03)	Blue	8257	162.933	155.231	4.841
	Green	7317	180.679	205.973	-13.083
	Red	9942	209.256	217.802	-4.002
	NIR	10656	158.853	162.925	-2.531
Libya-4 (2013/08/06)	Blue	7993	139.17	150.268	-7.668
	Green	7105	178.392	200.440	-11.640
	Red	9634	205.706	211.550	-2.801
	NIR	10279	153.479	157.571	-2.631

Monitoring Instrument (OMI) were also used as input data for simulating inverse computation of Landsat-8 OLI surface reflectance and direct radiative transfer of TOA reflectance of KOMPSAT-3. For the aerosol optical depth, a climatological analysis value of 0.2 [32] was used due to the absence of a reliable value for the test site.

Table VIII lists the radiometric results for TOA radiance comparison using radiometrically calibrated Landsat-8 with KOMPSAT-3 radiance from well-known surface tarps.

For most cross-calibration cases, a significant difference (in the excess of 30%) between Landsat-8 and KOMPSAT-3 was not detected, any exceptions including the green band and

cases where Algeria-3 during cross-validation. As shown in Table VIII, the Algeria-3 site showed the largest radiance difference between Landsat-8 OLI and calibrated KOMPSAT-3. We think that this is due to a geometrical coupling discrepancy between the two sensors. The Algeria-3 case has not only a high viewing zenith angle of $\sim30°$ but also a large solar zenith angle of $\sim60°$. The combination of these two provides poor cross-validation conditions. This indicates the importance of similar geometric conditions for cross-validation. Also, in the case of high solar zenith angles ($\sim60°$), bidirectional effects would create the principal source of uncertainty between Landsat-8 and KOMPSAT-3. However, the Libya-4 sites from 2013 to 2015 demonstrated similar geometric conditions but still showed reasonable accuracy, despite the inherent error associated with vicarious calibration. In 2013 at Libya-4, the accuracy was less than 10%, except at the green bands due to similar geometrical coupling conditions. As with the Algeria-3 sites, we feel that the geometrical discrepancy was the primary cause of reduced radiance accuracies at the Libya-4 sites. Finally, calibrated KOMPSAT-3 showed the reasonable cross-validation results in spite of approximate error budget of vicarious calibration with surface tarps of $\sim7\%$.

IV. CONCLUSION

KARI performed an initial assessment of a vicarious radiometric calibration of KOMPSAT-3 images using well-known surface tarps and found that radiance coefficients derived from the DNs consistently yielded reliable results. To obtain accurate surface reflectance values, field campaigns were performed using well-known surface tarps measured by ASD FieldSpec 3. Although precise ground measurements for aerosol, amount of water, and total ozone are required by atmospheric instruments, MODIS atmospheric products are also useful as input parameters for 6S model simulations.

In conclusion, the estimated radiometric characteristics of KOMPSAT-3 DNs to radiance produced reasonable results using well-known surface tarps. The rmse differences between simulated radiance and measured radiance during the second field campaign for "sensor-to-itself" calibration were 2.072 W/m^{2}sr (blue), 6.80 W/m^{2}sr (green), 7.512 W/m^{2}sr (NIR), and 5.712 W/m^{2}sr (red), respectively. This highlights that radiometric calibration with tarps is a reliable method. Furthermore, the gain ratio between the first and second field campaigns was $< 5\%$, indicating that the radiometric coefficients determined for KOMPSAT-3 are suitable for estimating continuous variables for quantitative applications. However, the approximate error budget of vicarious calibration for KOMPSAT-3 was $\sim7\%$, which indicates that improvements are still needed in our vicarious calibration methodology. Inherent vicarious calibration errors emerge when performing cross-validation of KOMPSAT-3 with radiometrically well-calibrated Landsat-8 over bright desert areas. The use of easily installed tarps and MODIS atmospheric products, rather than precise ground measurement, was thus a limitation of this study. However, the main purpose of the study was to characterize the radiometric status of KOMPSAT-3. In future work, KARI plans to conduct field campaigns by preparing accurate ground measurements, using laboratory BRDF measurements for correction, a sky radiometer, ozone meters, and a sunphotometer.

REFERENCES

[1] A. S. Belward, "International co-operation in satellite sensor calibration; the role of the GEOS working group on calibration and validation," *Adv. Space Res.*, vol. 23, no. 8, pp. 1443–1448, Jan. 1999.

[2] S. Liang, *Quantitative Remote Sensing of Land Surface.* New York, NY, USA: Wiley, 2004, pp. 178–194.

[3] J. J. Butler and R. A. Barnes, "Calibration strategy for the Earth Observing System (EOS)-AM1 platform," *IEEE Trans. Geosci. Remote Sens.*, vol. 36, no. 4, pp. 1056–1061, Jul. 1998.

[4] H. S. Chen, *Remote Sensing Calibration Systems: An Introduction.* Hampton, VA, USA: Deepak, 1997.

[5] M. Dinguirard and P. N. Slater, "Calibration of space-multispectral imaging sensors: A review," *Remote Sens. Environ.*, vol. 68, no. 3, pp. 194–205, Jun. 1999.

[6] O. Hagolle *et al.*, "Results of POLDER in-flight calibration," *IEEE Trans. Geosci. Remote Sens.*, vol. 37, no. 3, pp. 1550–1566, May 1999.

[7] W. A. Abdou *et al.*, "Vicarious calibration experiment in support of the multi-angle imaging spectroradiometer," *IEEE Trans. Geosci. Remote Sens.*, vol. 40, no. 7, pp. 1500–1511, Jul. 2002.

[8] D. X. Kerola, C. J. Bruegge, H. N. Gross, and M. C. Helmlinger, "On-orbit calibration of the EO-1 Hyperion and Advanced Land Imager (ALI) sensors using the LED Spectrometer (LSpec) automated facility," *IEEE Trans. Geosci. Remote Sens.*, vol. 47, no. 4, pp. 1244–1255, Apr. 2009.

[9] A. Kamei *et al.*, "Cross calibration of FORMOSAT-2 Remote Sensing Instrument (RSI) with Terra Advanced Spaceborne Thermal Emission and Reflectance Radiometer (ASTER)," *IEEE Trans. Geosci. Remote Sens.*, vol. 50, no. 11, pp. 1–11, Nov. 2012.

[10] C.-C. Liu *et al.*, "Vicarious calibration of the FORMOSAT-2 remote sensing instrument," *IEEE Trans. Geosci. Remote Sens.*, vol. 48, no. 4, pp. 2162–2169, Apr. 2010.

[11] S. B. Seo, "Relative compensation method for degradation of visible detectors using improved direct histogram specification," *Electron. Lett.*, vol. 50, no. 6, pp. 446–447, Mar. 2014.

[12] K. J. Thome, S. F. Bigger, and W. Wisniewski, "Cross comparison of EO-1 sensors and other Earth resources sensors to Landsat-7 ETM+ using Railroad Valley Playa," *IEEE Trans. Geosci. Remote Sens.*, vol. 41, no. 6, pp. 1180–1188, Jun. 2003.

[13] M. Pagnutti *et al.*, "Radiometric characterization of IKONOS multispectral imagery," *Remote Sens. Environ.*, vol. 88, no. 1/2, pp. 53–68, Nov. 2003.

[14] Korea Meteorology Agency Web Site. [Online]. Available: http://www.kma.go.kr/weather/climate/average_regional03.jsp

[15] C. G. Jin, H. S. Lim, and S. G. Lee, "Comparison of TOA reflectance calculated with images taken by KOMPSAT-3 and Landsat-8," in *Proc. ACRS*, Oct. 2013, vol. 823, pp. 1–5.

[16] E. F. Vermote, D. Tanré, J. L. Deuzé, M. Herman, and J. J. Morcette, "Second simulation of the satellite signal in the solar spectrum, 6S: An overview," *IEEE Trans. Geosci. Remote Sens.*, vol. 35, no. 3, pp. 675–686, May 1997.

[17] J. S. Hwang, "Absolute measurement of hyperspectral and angular reflection," *Appl. Opt.*, vol. 53, no. 27, pp. 6216–6221, Sep. 2014.

[18] G. T. Georqiev and J. J. Butler, "Laboratory-based bidirectional reflectance distribution functions of radiometric tarps," *Appl. Opt.*, vol. 47, no. 18, pp. 3313–3323, Jun. 2008.

[19] T. Feingersh, W. Dorigo, R. Richter, and E. Ben-Dor, "A new model-driven correction factor for BRDF effects in HRS data," in *Proc. EARSel Workshop*, Jan. 2005, pp. 502–511.

[20] G. Thuillier *et al.*, "The solar spectral irradiance from 200 to 2400 nm as measured by the SOLSPEC spectrometer from Atlas and Eureca missions," *Sol. Phys.*, vol. 214, pp. 1–22, May 2003.

[21] P. Henry, G. Chander, B. Fougnie, C. Thomas, and X. Xiong, "Assessment of spectral band impact in intercalibration over desert sites using simulation based on EO-1 Hyperion data," *IEEE Trans. Geosci. Remote Sens.*, vol. 51, no. 3, pp. 1297–1308, Mar. 2013.

[22] L. A. Remer *et al.*, "The MODIS aerosol algorithm, products, and validation," *J. Atmos. Sci.*, vol. 62, pp. 947–973, Apr. 2005.

[23] J. C. Andersion, J. Wang, J. Zeng, M. Petrenko, G. G. Leptoukh, and C. Ichoku, "Accuracy assessment of Aqua-MODIS aerosol optical depth over coastal regions: Importance of quality flag and sea surface wind speed," *Atmos. Meas. Technol.*, vol. 5, pp. 5205–5243, Jul. 2012.

[24] Y. J. Kaufman and B. C. Gao, "Remote sensing of water vapor in the near IR from EOS/MODIS," *IEEE Trans. Geosci. Remote Sens.*, vol. 30, no. 5, pp. 871–884, Sep. 1992.

[25] W. P. Menzel, S. W. Suzanne, J. Li, and L. E. Gumley, "MODIS atmospheric profile retrieval algorithm theoretical basis document," Nat. Aeronaut. Space Admin. (NASA), Washington, DC, USA, Oct. 2002.

[26] N. Pahlevan, Z. Lee, J. Wei, C. B. Schaaf, J. R. Schott, and A. Berk, "On-orbit radiometric characterization of OLI (Landsat-8) for applications in aquatic remote sensing," *Remote Sens. Environ.*, vol. 154, pp. 272–284, Nov. 2014.

[27] N. Mishre, M. O. Haque, L. Leigh, D. Aaron, D. Helder, and B. Markham, "Radiometric cross calibration of Landsat 8 Operational Land Imager (OLI) and Landsat 7 Enhanced Thematic Mapper Plus (ETM+)," *Remote Sens.*, vol. 6, pp. 12 619–12 638, Dec. 2014.

[28] H. Cosnefroy, M. Leroy, and X. Briottet, "Selection and characterization of Saharan and Arabian desert sites for the calibration of optical satellite sensors," *Remote Sens. Environ.*, vol. 58, no. 1, pp. 101–114, Oct. 1996.

[29] P. Henry, M. Dinguirard, and M. Bidilis, "SPOT multitemporal calibration over stable desert areas," in *Proc. SPIE Int. Symp. Aerosp. Remote Sens.*, Orlando, FL, USA, Apr. 12–16, 1993, pp. 67–76.

[30] F. Cabot, O. Hagolle, H. Cosnefroy, and X. Briottet, "Intercalibration using desertic sites as a reference target," in *Proc. Geosci. Remote Sens. Symp.*, Seattle, WA, USA, Jul. 6–10, 1998, vol. 5, pp. 2713–2715.

[31] S. Lachérade, B. Fougnie, P. Henry, and P. Gamet, "Cross calibration over desert sites: Description methodology, and operational implementation," *IEEE Trans. Geosci. Remote Sens.*, vol. 51, no. 3, pp. 1098–1113, Mar. 2013.

[32] Y. M. Govaerts and M. Clerici, "Evaluation of radiative transfer simulation over bright desert calibration sites," *IEEE Trans. Geosci. Remote Sens.*, vol. 42, no. 1, pp. 176–187, Jan. 2004.
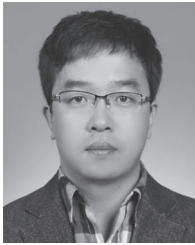
Jong-Min Yeom received the B.Sc. degree in atmospheric science, the M.S. degree in remote sensing, and the Ph.D. degree from Pukyong National University, Busan, South Korea, in 2003, 2005, and 2009, respectively.

His Ph.D. research focused on exploring the utility of satellite data sensed by sun- and geosynchronous satellites to retrieve land surface biophysical parameters including nadir BRDF-adjusted reflectance, vegetation indices, and surface insolation. He worked as a Postdoctoral researcher at Pukyong National University. He has been a Postdoctoral Research Associate with South Dakota State University, Brookings, SD, USA, since September 2009 under Prof. D. Roy. He is currently with the Korea Aerospace Research Institute, Daejeon, South Korea. His current work is on radiometric calibration and validation of onboard KOMPSAT series and involves monitoring vegetation, agriculture, solar energy resource, and surface albedo by using sun and geosynchronous satellites.

Jisoo Hwang received the M.S. degree in physics and the Ph.D. degree in optics from Ewha Womans University, Seoul, South Korea, in 1998 and 2005, respectively.

Her Ph.D. research was on optical characterization of nanostructures including photonic crystals, cholesteric liquid crystals, and nanomaterials. She was a Postdoctoral Fellow with the College of Optics and Photonics (CREOL), University of Central Florida, Orlando, FL, USA, in 2005–2006. She joined the Korea Research Institute of Standards and Science, Daejeon, South Korea, in 2007. Her current research interests include new metrology for optical material characterization and human visual perception.

Cheong-Gil Jin received the B.A. and Master's degrees of satellite information engineering from Pukyong National University, Busan, South Korea, in 2010 and 2012, respectively.

He studied GIS, computer, electronic, photogrammetry engineering, and remote sensing. He is currently a Researcher with Data Processing & Cal/Val Team, Korea Aerospace Research Institute, Daejeon, South Korea. His research theme is absolute/vicarious radiometric calibration and radiative transfer code.

Dong-Han Lee was born in Seoul, South Korea. He received the B.S., M.S., and Ph.D. degrees in astronomy and space science from Yonsei University, Seoul, in 1990, 1994, and 2011, respectively.

He has been a Chief Engineer of the Calibration and Validation for the KOMPSAT series of Korea Aerospace Research Institute (KARI), Daejeon, South Korea, since 1995. He is a Specialist of the radiometric and spatial calibration and validation of the high resolution optical remote sensing satellite and the Head of the Cal/Val & Data Quality Control Team, KARI.

Kyung-Soo Han received the Ph.D. degree from Laval University, Ville de Quebec, QC, Canada, in 2002, where his Ph.D. dissertation title is "Integration of GOES and NOAA Images for Hydrometeorological Applications" focused on satellite-based estimations of actual evapotranspiration and forest weather index.

From 2002 to 2004, he was a Postdoctoral for the studies related on BRDF modeling and Global Land Cover 2000 project (GLC2000) with Meteo-France, Toulouse, France. He is currently the Head Professor of the Department of Spatial Information Science, Pukyong National University, Busan, Korea. He is the Editor-in-Chief of the *Korean Journal of Remote Sensing*.